

Atmospheric components: analyzing Inpainting methods to removal these occurrences in remote sensing images

Ana Carolina Siravenha, Danilo Sousa, Aline Bispo, and Evaldo Pelaes *

Signal Processing Laboratory, Federal University of Para (UFPA), Belem, PA, Brazil.
{siravenha,danilofrazaopelaes}@ufpa.br, aline.bispo@itec.ufpa.br

Abstract

This paper presents the evaluation of two approaches, widely used in the inpainting literature, applied in the context of the atmospheric noise removal, such as fog, clouds - dense and sparse - and shadows, which often occur in remote sensing images. The presence of such elements affect, in many ways, the image processing in an environmental or urban monitoring, and also in the steps of the digital image processing, suchlike segmentation and classification. Whilst one approach uses a technique of interpolation for the dissemination of information by a multidimensional Discrete Cosine Transform (DCT) smoothing method, the other one is based on second-order partial differential equations methods (PDE). This PDE-based development uses the heat diffusion and thin-plate spline methods to achieve their solutions with the aid of the finite-difference method. To proceed the methods evaluation, this work uses the kappa coefficient and the Peak Signal-to-Noise Ratio index (PSNR). The metrics indicate the effectiveness of the DCT strategy, which produces higher quality images, specially when comparing the results obtained by the use of differential equations modeled by thin-plate spline. The visual aspect of images is clearly an important factor for measuring the effectiveness of any image processing, so, in addition to numerical metrics, are presented the nine images used to evaluate both methods.

Keywords: *Inpainting, Cloud removal, DCT, Heat diffusion.*

1 Introduction

Remote sensing images are usually susceptible to the undesirable presence of the atmospheric interferences, such as fogs, clouds and haze. These occurrences, that are largely present in equatorial and tropical warm-to-hot regions, changes the brightness values of pixels at different levels of saturation, which can corrupt the visual representation of the land surface that is covered by clouds. The presence of such elements affect, in many ways, the image processing in an environmental or urban monitoring, and also the segmentation and/or classification methods that are the mainly responsible for the image information extracting.

Experts worldwide carried out many studies in order to find an effective method to reduce or eliminate the impact of clouds [30]. Algorithms dedicated to the satellite images processing should be robust in the sense that this kind of image usually has large dimensions and large spectral variations (very heterogeneous). In this sense, the encouragement to develop new alternatives for image interpretation and improvement of efficient known techniques is remarkable.

The method used in treatment of the atmospheric interferences vary according to the clouds density. It can be dense or thin.

When it comes to the removal of scattered clouds, mist and fog, considered smooth structures, shown in Figures 1 (a), the most or widely used technique is the application of the homomorphic

*This work was supported by *Fundação de Amparo à Pesquisa do Estado do Pará*, grant no. 021/2008, *Desenvolvimento de um sistema de interpretação de imagens de satélite baseado em modelos híbridos.*

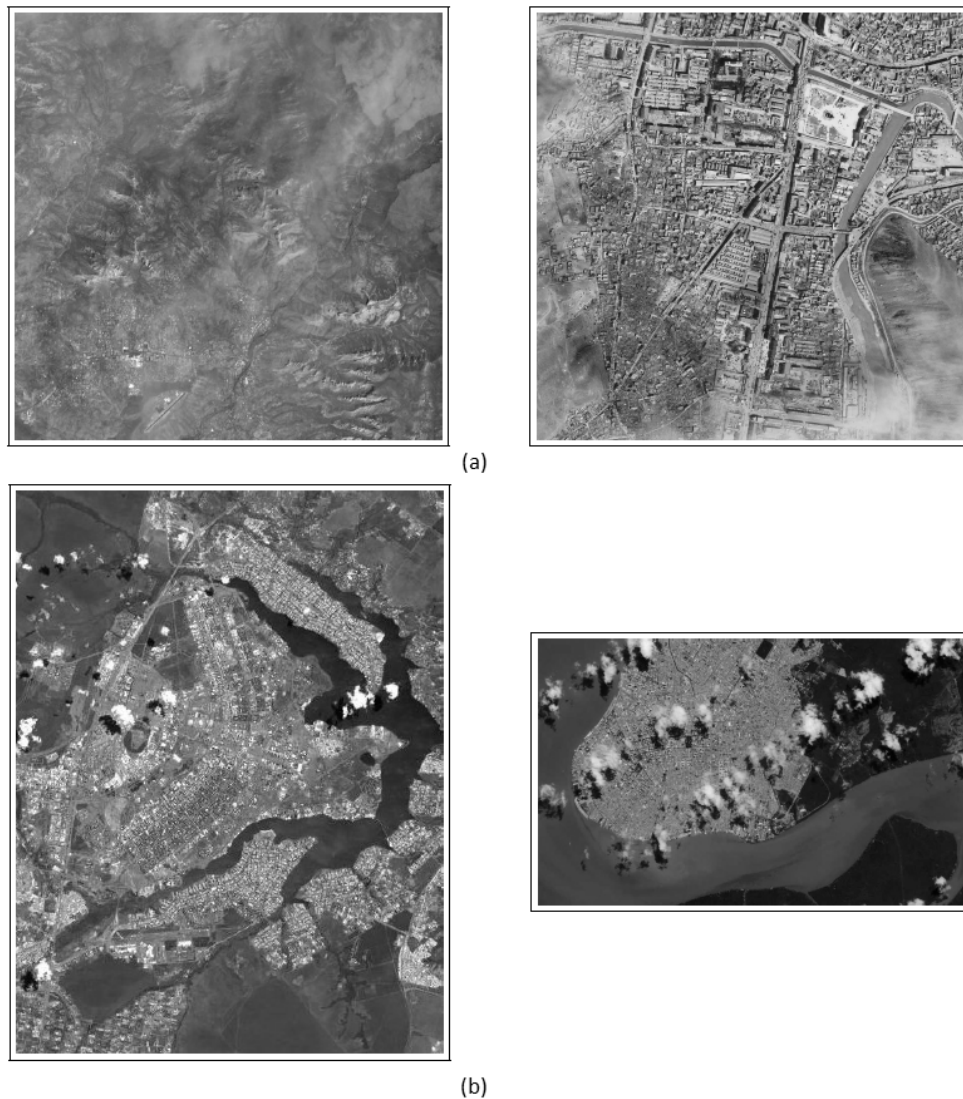


Fig.1. Examples of images contaminated with atmospheric structures: (a) thin clouds, mists and fogs and (b) dense clouds and shadows.

filter in regions where such components predominate, working in the frequency components and applying some kind of high-pass filter in the image, as made in [18] and [13].

The dense clouds and shadows [illustrated in Figure 1 (b)] removal is mainly related to the use of reference images or by the estimative of the covered areas. The first strategy can use a multi-temporal analysis [30], or can use an other image of the same scene, captured by a different sensor, as a SAR image [14], both aims to make the interpolation of the affected area. This interpolation can use similar techniques to those described in [8,17]. These works developed derivations of the *inpainting* method in order to fill up some damaged regions or to remove large objects.

In the literature, inpainting techniques are increasingly used in benefits of the satellite images processing. In [19], is effectively used a technique based on Bandelet transformed with a multi scale geometrical grouping in clouds removal of images.

Some authors prefer the *a priori* knowledge approaches as [23,24], which are based on the maximum *a posteriori* (MAP) algorithm. In MAP, the likelihood probability density function (PDF) is built on a linear observation model of the image, and a robust model of *Huber-Markov* is used as

an *a priori* PDF. It is common in this area, researches reporting the reconstruction of images of specific sensors, as done by [14], who works in removing the cloud of images produced by *ALOS* satellite sensors.

In this work two *inpainting* based approaches are evaluated. We are interesting in the removal of the dense clouds and shadows present in satellite images. The presence of dense clouds are related to the presence of the shadows, formed principally by the sun position in the moment of capture and because the image capture in off-nadir angle.

The first approach uses a multidimensional Discrete Cosine Transform (DCT) based smoothing method, similar to those described in [10, 1, 3], whilst the other approach is based in Partial Differential Equations, that are modeled by two methods: the heat diffusion and thin-plate spline [6, 4, 21].

In the sequence are described the techniques used in the approaches, Section 2, the results achieved and it is discussions, Section 3. At last, we present the work conclusions (Section 4).

2 Methodology

Before apply the cloud removal routines, the image is submitted to a region detection method. The basis of this clouds and shadows detection process is introduced in [13], where is made a separation of regions with different features in the image, to then effectively apply the processing techniques in their respective target regions. This separation is made according to statistical measures of the image, detecting areas of dense clouds, thin clouds and areas not exposed to any of these types of noise.

In [25], was added the ability to detect clouds and shadows (mainly originating from the angle of capture of the image), and two constants *sc* (shadow constant) and *cc* (cloud constant), that allowed a greater flexibility to the task of regions separating with different illumination levels. The function that represents this process is presented in Equation 1. It is important highlight that this equation is applied to all bands of the image. For example, a pixel in *dim* dimensions is considered as a region of shadow if in all *l_{dim}* bands has its gray level value less than the multiplication between the *cc* constant and the value of the subtraction of the pixels average value and the standard deviation of the image.

$$l_{dim}(x, y) = \begin{cases} i(x, y) < sc \times i_{m-dp}, & i(x, y) \in 0, \\ i_{m-dp} < i(x, y) < i_m, & i(x, y) \in 1, \\ i_m < i(x, y) < cc \times f_{m+dp}, & i(x, y) \in 2, \\ i(x, y) > cc \times i_{m+dp}, & i(x, y) \in 3. \end{cases} \quad (1)$$

Where *i(x, y)* is an original image pixel, *i_m* and *i_{dp}* represents the mean and standard deviation values of the image pixels, respectively, the function *l_{dim}(x, y)* is a mapped matrix that have the same dimension of the original image. The image *l(x, y)* have four values (0, 1, 2 and 3), where the mapped regions as 0 corresponds to the shadows areas; the pixels mapped as 1 represents regions without atmospheric damages detected; the regions damaged with clouds are divided in regions with thin clouds (2) and dense clouds (3).

Then, a morphological opening operation is applied on the image *l_{dim}*, extinguishing small objects contained in larger ones, since small objects contained in large blocks defined as noise can interfere with the step of applying methods used in this work. Thus, it is advisable to make the opening step after the regions detection, eliminating this problem and generating a better restoration of image pixels damaged by atmospheric action.

The restoration of degraded areas of images without prior knowledge of the original scene is a practice as old as the creation of art itself. This practice is called retouching or inpainting. The goal of inpainting is to redefine the parts that are missing or are damaged, in order to make it more readable, restoring their original units. In this work, the regions of shadows and dense clouds will be interpolated by the inpainting methods.

It is noticeable that the classical algorithms for noise removal of image does not apply to inpainting. In common applications of image enhancement, pixels contains information about the real data and noise (e.g., image plus noise for additive noise), while in the inpainting there is no significant information about the region to be redefined. The information is obtained mainly from the regions surrounding the areas to be processed. So then comes the need to develop specific techniques to solve these problems.

2.1 First approach

The interpolation process depends of the neighborhood of the pixels labeled as 0 and 3. These pixels, are redefined to $p = NaN$, which has two neighborhood (horizontal and vertical) described as $(x + 1, y)$, $(x - 1, y)$, $(x, y + 1)$ and $(x, y - 1)$, respectively. Besides these, there are other two diagonal neighborhoods $(x - 1, y - 1)$, $(x - 1, y + 1)$, $(x + 1, y - 1)$ e $(x + 1, y + 1)$. These neighborhood are illustrated by the Fig. 2(a) and Fig. 2(b).

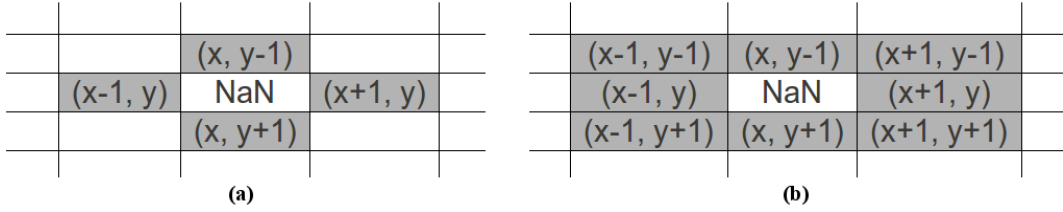


Fig. 2. NaN pixels neighborhood.(a) 4-neighborhood (b) 8-neighborhood [11].

2.1.1 Method A.1

In this method, the regions with dense clouds and shadows are reconstructed based on a formulation of a Partial Differential Equation (PDE). These equations contains unknown multivariable functions and their partial derivatives and are user to formulate problems involving functions of several variables. PDEs find their generalization in stochastic partial differential equations.

The PDE used in this work is modeled as a heat diffusion, where its approximation is given by a finite differences. It is applied a two-dimensional Laplacian elliptic equation to the linear equation system be resolved [27]. According [11], the most simple isotropic derivative operator is the Laplacian, expressed by the Eq. 2, where the function $f(x, y)$ describes a two-dimensional matrix.

$$\nabla^2 f = \frac{\partial^2 f}{\partial x^2} + \frac{\partial^2 f}{\partial y^2} = 0. \quad (2)$$

To an arbitrary number of undefined pixels n , there are n system equations. The Laplacian operator is linear to any order derivatives, and in discrete form, the equation, on the x direction, is defined as

$$\frac{\nabla^2 f}{\nabla x^2} = f(x + 1, y) + f(x - 1, y) - 2f(x, y), \quad (3)$$

and, on the y direction, as

$$\frac{\nabla^2 f}{\nabla y^2} = f(x, y + 1) + f(x, y - 1) - 2f(x, y). \quad (4)$$

Replacing the Eq. 3 and 4 on the Eq. 2 is obtained the discrete Laplace equation

$$\begin{aligned} \nabla^2 f(x, y) &= f(x + 1, y) + f(x - 1, y) \\ &+ f(x, y + 1) + f(x, y - 1) - 4f(x, y). \end{aligned} \quad (5)$$

Considering that in Eq. 5 the coefficients are representing the pixels in its spatial form, as showed in Fig. 3, it will be the central pixel redefined by the average of the weights of its neighbors [9].

	0	1	0
1		-4	1
0		1	0

Fig. 3. Coefficients in spatial domain [11].

The linear equations systems are formulated by the undefined pixel neighborhood, according to the illustrated in Fig. 2(a). The system solution gives the values attributed to the undefined pixel.

This method propagates the smooth information of the edge to the regions identified as containing shadow or dense cloud. To small regions, this method is more efficient, supposing that the high frequency elements (typical of the edges) are not totally damaged by the atmospheric noise.

2.1.2 Method A.2

The second method follows the same proceedings of the method A.1, but in this case, the PDE uses the neighborhood illustrated in Fig. 4.

		(x,y-2)		
	(x-1, y-1)	(x, y-1)	(x+1, y-1)	
(x-2,y)	(x-1, y)	NaN	(x+1, y)	(x+2,y)
	(x-1, y+1)	(x, y+1)	(x+1, y+1)	
		(x,y+2)		

Fig. 4. Neighborhood of the undefined pixel (NaN) in method A.2.

According [9], the differential equation model described in this work is more appropriated to a thin-plate spline model than the heat diffusion model. Spline interpolation technique estimates the unknown data among known data. Thin-plate spline PDE is a scalar function expressed as a linear combination of shifted samples of the kernel function added to the polynomial term, and can be described as

$$f(x, y) = a_1 + a_x x + a_y y + \sum_{i=1}^N w_i \Phi(|P_i - (x, y)|), \quad (6)$$

where N is the number of the pixels in an image, Φ is called the fundamental solution defined as a function $z(x, y) = -\Phi = -r^2 \log(r)$ over the (x, y) plan, where r is the Euclidean distance to the Cartesian origin [7, 20]. Given N points with known coordinates $P_1 = (x_1, y_1)$, $P_2 = (x_2, y_2)$, \dots , $P_N = (x_N, y_N)$ of the image it is possible calculate $r_{ij} = |P_i - P_j|$ between i and j points. The coefficients a_1 , a_x e a_y are coefficients calculated on the basis of homologous points [20].

The thin-plate spline method is based on the fundamental solution of a biharmonic equation (Φ) that models a metal thin plate over the two-dimensional signal [20]. The mapping of regions to be restored is driven by energy minimization of curvature of a thin plate of metal, tending to an almost linear behavior as the neighborhood points become more distant from the undefined [5].

The two-dimensional function $f(x, y)$ is divided into two parts: a sum of functions $\Phi(r)$ of a lightly flat surface and other part that expressing affine transformation, representing the behavior of $f(x, y)$ at infinity [2].

To map regions corrupted by clouds is necessary to solve a system of equations formed by the Equations 7, 8 and 9 restricted to the conditions described in [7, 20]:

$$\sum_{i=1}^N w_i = 0, \quad (7)$$

$$\sum_{i=1}^N w_i x_i = 0, \quad (8)$$

$$\sum_{i=1}^N w_i y_i = 0. \quad (9)$$

These conditions ensure that the sum of the weights w_i are null, and the multiplication by the P_i coordinates (x, y) also are null [20]. The matrix K of dimension $N \times N$ that is a $\Phi(r)$ function is defined as follows:

$$K_{N \times N} = \begin{bmatrix} 0 & \Phi(r_{12}) & \dots & \Phi(r_{1N}) \\ \Phi(r_{21}) & 0 & \dots & \Phi(r_{2N}) \\ \dots & \dots & \dots & \dots \\ \Phi(r_{N1}) & \Phi(r_{N2}) & \dots & 0 \end{bmatrix}. \quad (10)$$

A matrix P of dimension $N \times 3$ is constructed through points coordinates:

$$P_{N \times 3} = \begin{bmatrix} 1 & x_1 & y_1 \\ 1 & x_2 & y_2 \\ \dots & \dots & \dots \\ 1 & x_N & y_N \end{bmatrix}. \quad (11)$$

Based on the K and P matrices, it can compose the matrix called L with dimension $(N + 3) \times (N + 3)$:

$$L_{(N+3) \times (N+3)} = \left[\begin{array}{c|c} K & P \\ \hline P^T & O \end{array} \right], \quad (12)$$

where O is a null matrix 3×3 .

Combining the N homologous points $P'_1 = (x'_1, y'_1)$, $P'_2 = (x'_2, y'_2)$, \dots , $P'_N = (x'_N, y'_N)$, the matrix V of dimension $2 \times N$ can be constructed [20]:

$$V_{2 \times N} = \begin{bmatrix} x'_1 & x'_2 & \dots & x'_N \\ y'_1 & y'_2 & \dots & y'_N \end{bmatrix}. \quad (13)$$

The matrix Y is obtained by adding three columns to the matrix V with zero values:

$$Y_{(N+3) \times 2} = (V | 0 \ 0 \ 0)^T. \quad (14)$$

Multiplying the inverse of the matrix L with the matrix Y is possible obtain a new matrix containing the coefficients $w_1, w_2, \dots, w_N, a_1, a_x$ and a_y , used in the method.

$$W = L_{N+3}^{-1} Y_2 = (w_1 \ w_2 \ \dots \ w_N \ a_1 \ a_x \ a_y)^T. \quad (15)$$

Each column of the matrix $L^{-1}Y$ provides the coefficients w_i to the mapping function in one component (x and/or y) [20].

Because the model uses the relative distance between the points, some numerical problems can occur. Points too much distant or too much closer causes rows or column linearly dependents (or almost that) in a K matrix, consequently, this matrix becomes ill-conditioned and its inverse becomes unstable [20].

2.2 Second approach

This method was proposed by [10], and so as in [1], is based on information propagation by smoothing, from the regions surrounding one where the data needs to be redefined. The specificity of this approach is related to the use of the Discrete Cosine Transform (DCT) and its inverse to simplify and solving linear systems, producing an efficient smoothing.

2.2.1 Smoothing by Penalized Least Squares Regression

In statistics and data analysis, smoothing is used to reduce experimental noise or information on a small scale and keeping the most important marks of a data set. Consider the following model for the one-dimensional noisy signal y from the Eq. 16.

$$y = \hat{y} + \varepsilon, \quad (16)$$

where ε represents a Gaussian noise with zero mean and unknown variance, and \hat{y} is the so-called smoothing, i.e., has continuous derivatives up to some order (usually ≥ 2) throughout the domain. The smoothing of y depends on the best estimate of \hat{y} and this operation is usually performed by parametric or nonparametric regression.

A classic approach to smoothing is the penalized least squares regression. This technique consists in minimizing a criterion that balances fidelity to the data, measured by the residual sum-of-squares (RSS) and a penalty term (P), which reflects the robustness of the smoothed data. So, the Eq. 17 should be minimized.

$$F(\hat{y}) = RSS + sP(y) = \| \hat{y} - y \|^2 + sP(y), \quad (17)$$

where $\|\cdot\|$ is the Euclidean norm. The parameter s is a positive real scalar that controls the grade of smoothing, so that, as it increases, the degree of smoothing of \hat{y} increases too. When the Robustness penalty is written in terms of the integral square of the p -th derivative of \hat{y} , the penalized regression is known as smoothing spline.

Another simple and straightforward approach to express the robustness is by using a second-order divided difference, which produces an one-dimensional array of data, shown in Eq. 18

$$P(\hat{y}) = \| D(\hat{y}) \|^2, \quad (18)$$

where D is a three-diagonal square matrix defined by

$$D_{i,i-1} = \frac{2}{h_{i-1}(h_{i-1} + h_i)}, D_{i,i} = \frac{-2}{h_{i-1}h_i}, D_{i-1,i} = \frac{2}{h_i(h_{i-1} + h_i)}, \quad (19)$$

for $2 \leq i \leq n-1$, where n is the number of elements of \hat{y} and h_i is the step size between \hat{y}_i and \hat{y}_{i+1} .

Assuming repeated edge elements ($y_0 = y_1$ e $y_{n+1} = y_n$), it follows that

$$-D_{1,1} = D_{1,2} = \frac{1}{h_1^2}, D_{n,n-1} = -D_{n,n} = \frac{1}{h_{n-1}^2}. \quad (20)$$

These boundary conditions lead to further numerical simplifications involving evenly spaced data, as an image.

Now, using Eq. 17 and Eq. 18, the minimization of $F(\hat{y})$ results in a linear system expressed in Eq. 21, which allows the smoothed data determination.

$$(I_n + sD^T D)\hat{y} = y, \quad (21)$$

where I_n is the identity matrix $n \times n$ and D^T represents the transpose of D . Since $(I_n + sD^T D)$ is a penta-diagonal symmetric matrix, the last equation can be solved numerically in a computationally efficient way.

2.2.2 Smoothing Equally Spaced Data

The Eq. 21 can be solved using the so-called left division matrix applied to sparse matrices. Solving this linear system, however, can be time consuming for a large amount of data. This algorithm can be greatly simplified and accelerated if the data are evenly spaced, a situation that occurs in images, where pixels are equally spaced.

An efficient algorithm for smoothing uniformly sampled data is described in this section. Assuming now that the data are equally spaced with $h_i = 1 \forall i$, the divided differences matrix D (Eq. 21) can be rewritten as a simple difference matrix

$$D = \begin{pmatrix} -1 & 1 & & & \\ 1 & -2 & 1 & & \\ & \ddots & \ddots & \ddots & \\ & & 1 & -2 & 1 \\ & & & 1 & -1 \end{pmatrix}. \quad (22)$$

A self-decomposition of D yields

$$D = U \Lambda U^{-1}, \quad (23)$$

being Λ the diagonal matrix containing the self-values of D defined by

$$\Lambda = \text{diag}(\lambda_1, \dots, \lambda_n), \quad (24)$$

where $\lambda_i = -2 + 2 \cos((i-1)\pi/n)$. Since U is an unitary matrix, i.e. $(U^{-1} = U^T$ e $UU^T = I_n$) Eq. 21 leads to

$$\hat{y} = U(I_n + s\Lambda^2)^{-1}U^T y \equiv U\Gamma U^T y. \quad (25)$$

The components of the diagonal matrix Γ , according to Eq. 24, are given by:

$$\Gamma_{i,j} = [1 + s(2 - 2 \cos((i-1)\pi/n))^2]^{-1}. \quad (26)$$

taking $\Gamma_{i,j} = 0$ if $i \neq j$. Note that U^T and U are actually the type 2 matrices $n \times n$ of the DCT and its inverse, respectively, as observed in [26]. Thus, the output smoothing \hat{y} can also be expressed as:

$$\hat{y} = U\Gamma DCT(y) = IDCT(\Gamma DCT(y)), \quad (27)$$

where DCT and $IDCT$ refer to the Discrete Cosine Transform and its inverse, respectively.

It is more convenient to use an algorithm based on Eq. 27, instead of Eq. 21, when the data are equidistant. DCT has a computational complexity of $O(n \log(n))$, while Eq. 21, which requires a Cholesky factorization, has computational complexity of $O(n^3)$.

As described in [10], the task of smoothing can be performed by an iterative process to ensure greater convergence of the process, as shown in Eq. 28. Can also be seen that when there are undefined values in the image, smoothing is also responsible for interpolation of data, functioning as an inpainting method.

$$\hat{y}_{k+1} = IDCT(\Gamma DCT(y_k)). \quad (28)$$

Where k is the number of iterations.

2.2.3 Multidimensional Smoothing

Whereas multidimensional DCT is basically a composition of one-dimensional DCTs along each dimension, Eq. 28 can be immediately extended to equally spaced data in two (for images), or up to N dimensions, as shown in [3]. In general terms, to a N -dimensional data, the Eq. 28 becomes

$$\hat{y}_{k+1} = IDCTN(\Gamma^N \circ DCTN(y_k)). \quad (29)$$

Where \circ is the Schur product (element-to-element), while, Γ^n , represents a tensor of rank N defined by

$$\Gamma^n = 1^N \div (1^N + s \wedge^n \circ \wedge^n). \quad (30)$$

Here, the operator \div symbolizes the division element by element, and 1^N is a tensor of rank N composed by 1's. \wedge is the following tensor of rank N [3]

$$\wedge_{i_1, \dots, i_N}^N = \sum_{j=1}^N \left(-2 + 2 \cos \frac{(i_j - 1)\pi}{n_j} \right), \quad (31)$$

where n_j denotes the size of \wedge^n along the j -th dimension.

2.2.4 Specification of the inpainting technique used

In order to accelerate the convergence, the proposal of [10] starts the process by performing nearest neighbor interpolation on the image to be restored.

The nearest neighbor interpolation takes a points x to be interpolated and a few other neighbor points x_k , which are a sample portion of an image f_k . It is calculated the Euclidean distance among the value to be estimated and its neighbors, according following equation

$$d_k = \|x - x_k\|. \quad (32)$$

The value of x_k that produces the lower value of d_k has its intensity information attributed to x point. This measure repeats until to fulfill all undefined pixels [12].

Summarizing, for the inpainting performing in this work, initially is applied the nearest neighbor interpolation, following is used iteratively the Eq. 29 for two-dimensional data, i.e., $N = 2$. As proposed by [10], the smoothing parameter is set at 3, for which we obtain better results.

3 Results and Discussions

The methods evaluation has been done by its application on 9 satellite images from different sensors, with visible areas damaged with dense clouds and shadows. Following, the methods efficiency was numerically measured according the Kappa coefficient, which is based on the confusion matrix of the sample image [13]. To complete the evaluation was computed the Peak Signal-to-Noise (PSNR) index, which is based on the information similarity between the reference image and the interpolated image [22, 15].

To produces the reference or ground-truth images, the original damaged images has the atmospheric noises manually removed, simulating an optimal one, allowing the methods evaluation.

Firstly, was compared the A.1 and A.2 method, the both methods that use PDE in their formulations. The Table 1 shows that the A.1 method was superior than A.2 method, according the adopted criteria. The execution time of the method based in heat diffusion is considerably lower than thin-plate spline based method. As showed in Fig. 6 to Fig. 5, is evidenced the visual quality produced by the A.1 method (Fig. 6(c) to Fig. 5(c)) over the A.2 method results. Whilst, the images produced by the A.2 method presented noisily results, as showed in Fig. 6(b) to Fig. 5(b).

Table 1. Numerical evaluation considering the PDE-based methods. The PSNR index is given in dB .

Image	A.1 method		A.2 method	
	Kappa	PSNR	Kappa	PSNR
1	0.7608	24.62	0.3917	17.29
2	0.6941	25.02	0.5805	20.27
3	0.4449	21.15	0.3493	19.09
4	0.8329	30.25	0.3873	19.52
5	0.8173	28.94	0.8105	26.38
6	0.6442	25.68	0.6603	24.546
7	0.7440	28.40	0.6901	24.870
8	0.7572	22.36	0.6854	20.40
9	0.7624	28.34	0.7183	26.39

Associating numerical and visual factors, the A.2 method shows as an unfeasible algorithm to atmospheric noise removal, presenting white and black spots, that represents integer values too much larger or smaller than their neighbors. Concludes that the Laplacian function of the image intensity becomes too much larger around the noisily pixels, furthermore, the function associated to the diffusion coefficient is set to decrease quickly to preserves its edges. This effect is clearly noted, in Fig. 13(b) and in Fig. 5(b), principally.

The function related to the finite differences equation solution has small values around the noisily pixels, therefore, the spots tends to damage the images, as well observed in [28].

Table 2. Numerical evaluation of the methods PDE-based (A.1) and DCT-based (B). The PSNR index is given in dB .

Image	A.1 method		B method	
	Kappa	PSNR	Kappa	PSNR
1	0.7608	24.62	0.7566	23.67
2	0.6941	25.02	0.6935	24.98
3	0.4449	21.15	0.4435	20.95
4	0.8329	30.25	0.8232	29.41
5	0.8173	28.94	0.8120	28.61
6	0.6442	25.68	0.6414	25.56
7	0.7440	28.40	0.7375	28.30
8	0.7572	22.36	0.7531	22.53
9	0.7624	28.34	0.7622	28.34

Finally, comparing the A.1 and B methods, observing the Table 2, both methods have similar performance. The methods efficiency is also similar in the visual results, as showed in Fig. 6(c) and Fig. 6(d) to Fig. 5(c) and Fig. 5(d).

As well the other inpainting methods, the approaches studied in this work do not fulfill larger damaged regions, these reconstructed areas tend to becomes blurred and without texture information [16,8]. This fact is explained by the only use of the edge pixels information in diffusion. Examples are noted in Fig. 13, Fig. 12, Fig. 10 and Fig. 7, which have large areas damaged with dense clouds, in contrast with the Fig. 6 and 5 that present smaller undefined regions. In this figures it is possible note that in higher damage areas is generated homogeneous spots without texture information when large areas are interpolated.

The Fig. 12, Fig. 10 and Fig. 7 suffer from the presence of large amount of dense clouds. However, the case of the latter is worse, due to the excess of these elements, the resulting image from the

inpainting process becomes almost completely filled with information that is clearly unrealistic. The Fig. 12, cloud regions to be removed are over rough texture area (urban area), interfering in the inpainting process.

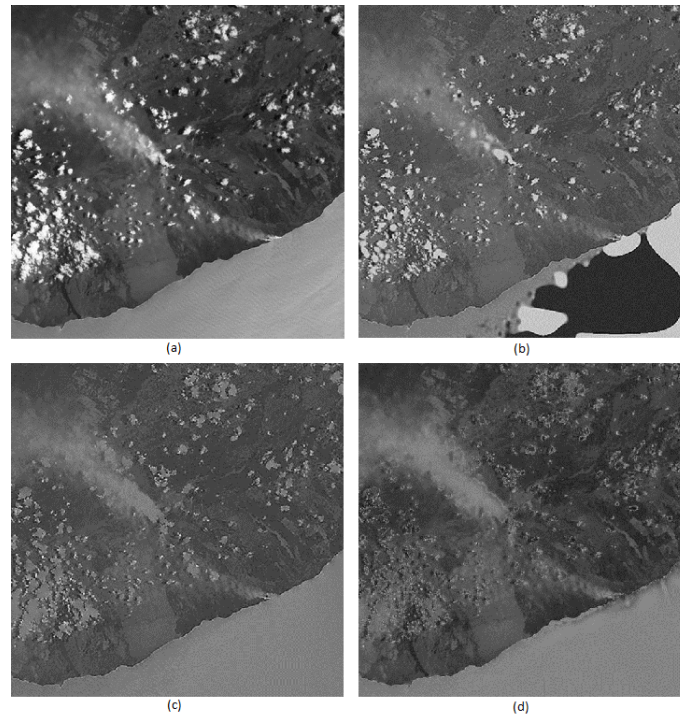


Fig. 5. (a)Image 1 of the Table 1 (b)Visual aspect produced by A.2 method (c)Visual aspect produced by A.1 method (d)Visual aspect produced by B method.

In another case, Fig. 8, Fig. 9 and Fig. 11 show dense clouds surrounded by scattered clouds, which also complicates the process of inpainting. Since the nearest neighbor, or the pixels surrounding these dense regions, are used in propagation of the information which produces some homogeneous spots in place of these areas.

On the other hand, Fig. 6 and Fig. 5 have predominantly small blocks of clouds, which are redefined in a more efficient way, since they are more suitable for the inpainting operation. According as illustrated, Fig. 5 contains a dense cloud area surrounded by scattered clouds, suffering the same problems mentioned, but with regards to the visual results of inpainting, it is the image that the B method visibly overcomes the A.1 method.

Generalizing, in Figures (b) are noted the result of ill-conditioned regions viewed in black and white areas, which makes the method unreliable for the restoration of the image, given the instability that can be generated by the matrix Φ , which depends of the reference region geometry in relation to the indefinite point. The discrepancy between the restored image and the image reference to the quantitative results evaluated by the Kappa coefficient and PSNR index presented low performance of the A.2 method in compared to the A.1 and B methods.

In the case of Figures (c), there is a spread of smoothness of neighboring pixels to the region of restoration, which compromises the restoration of areas of high frequency, typically edges. In [29], for instance, was carried out the combination of heat diffusion with isotropic diffusion to better control the flow of information.

The results, metric and visual, obtained by A.1 (Figures (c)) are similar to the method B (Figures (d)). There is a lack of texture on the restored areas, despite the smoothing parameter to be defined by the multidimensional DCT, which can extract texture features dominant.

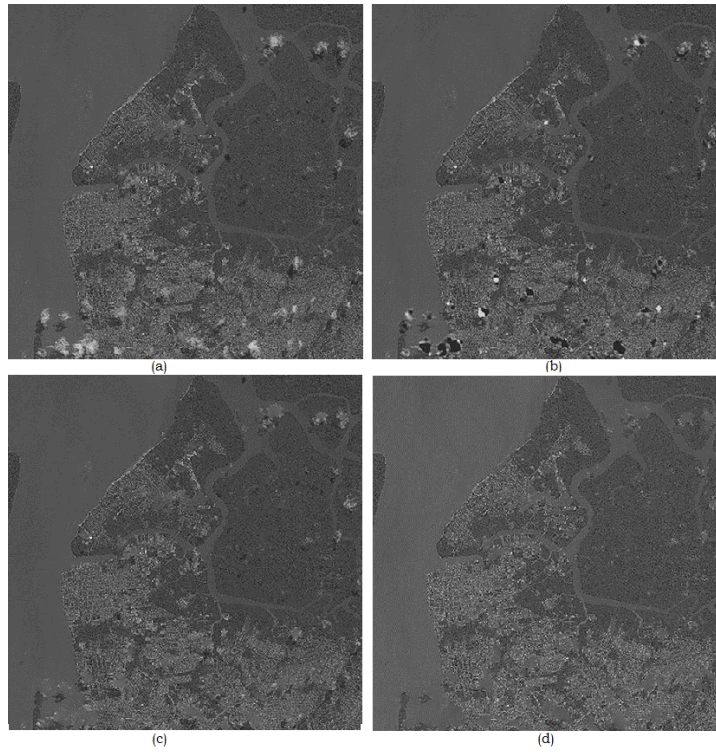


Fig. 6. (a)Image 2 of the Table 1 (b)Visual aspect produced by $A.2$ method (c)Visual aspect produced by $A.1$ method (d)Visual aspect produced by B method.

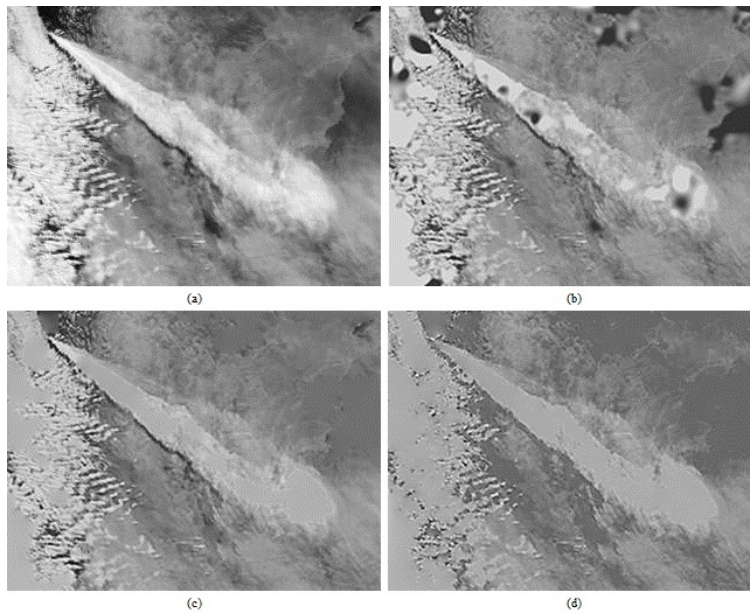


Fig. 7. (a)Image 3 of the Table 1 (b)Visual aspect produced by $A.2$ method (c)Visual aspect produced by $A.1$ method (d)Visual aspect produced by B method.

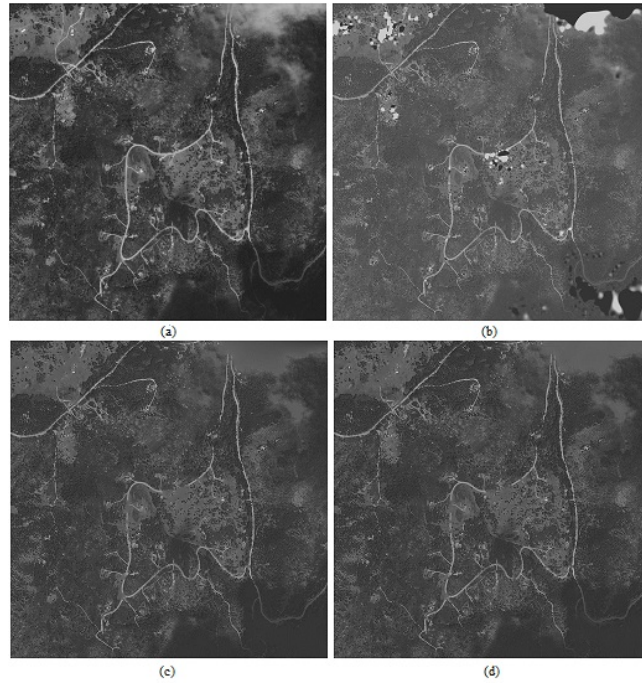


Fig. 8. (a)Image 4 of the Table 1 (b)Visual aspect produced by $A.2$ method (c)Visual aspect produced by $A.1$ method (d)Visual aspect produced by B method.

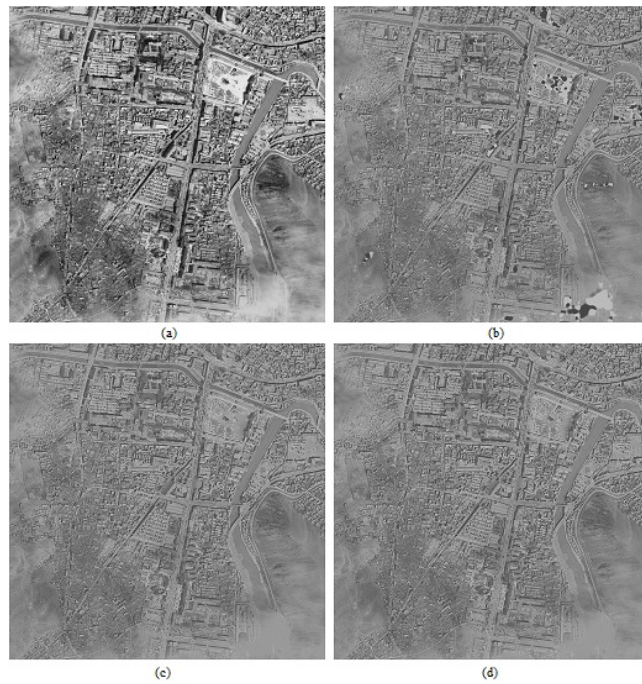


Fig. 9. (a)Image 5 of the Table 1 (b)Visual aspect produced by $A.2$ method (c)Visual aspect produced by $A.1$ method (d)Visual aspect produced by B method.

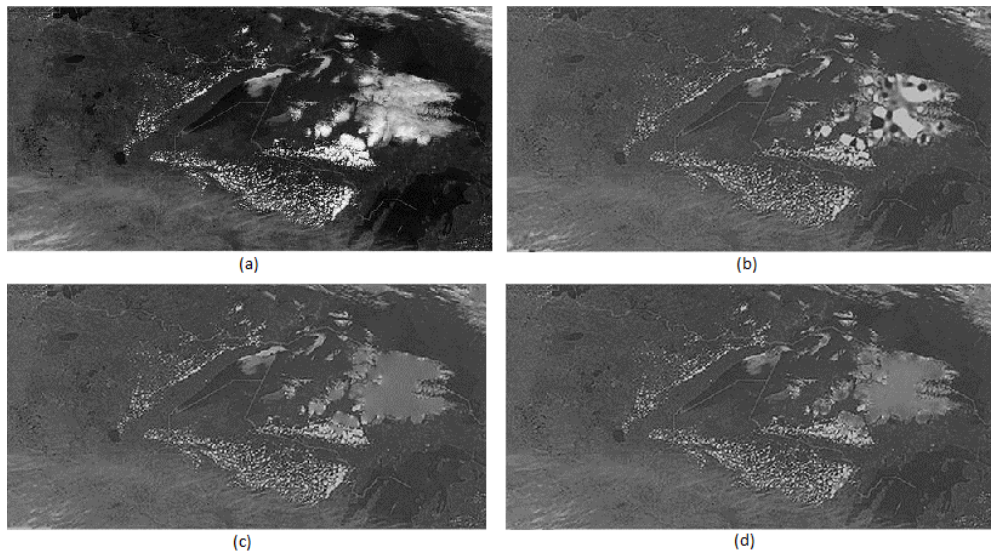


Fig. 10. (a)Image 6 of the Table 1 (b)Visual aspect produced by $A.2$ method (c)Visual aspect produced by $A.1$ method (d)Visual aspect produced by B method.

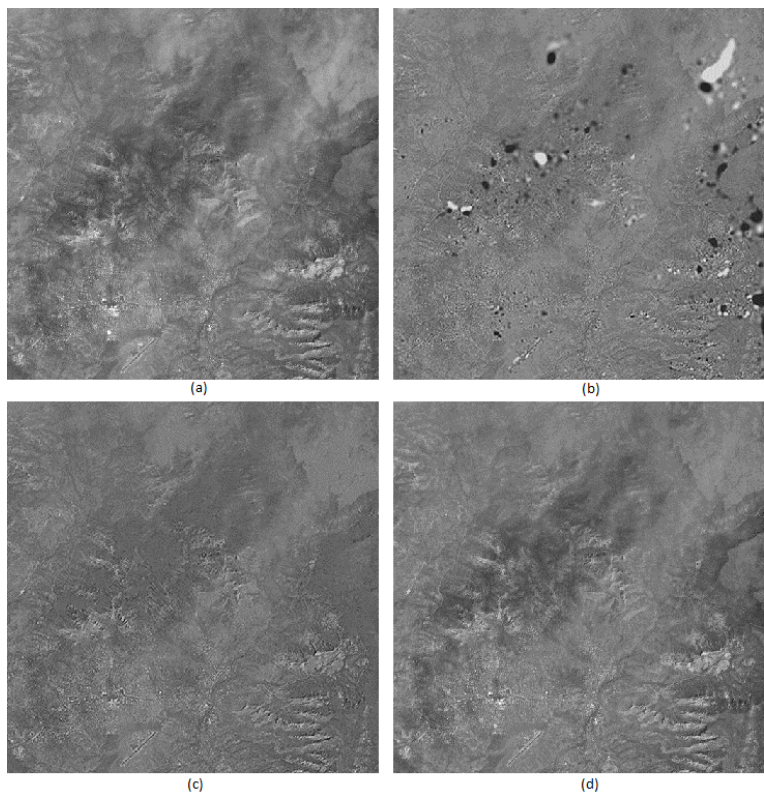


Fig. 11. (a)Image 7 of the Table 1 (b)Visual aspect produced by $A.2$ method (c)Visual aspect produced by $A.1$ method (d)Visual aspect produced by B method.

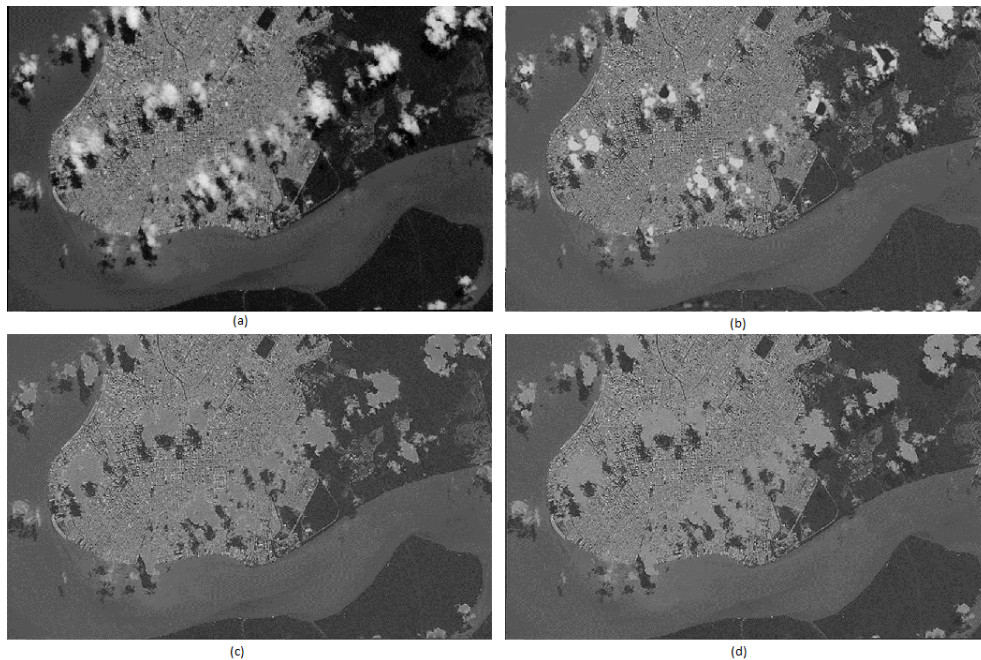


Fig. 12. (a)Image 8 of the Table 1 (b)Visual aspect produced by $A.2$ method (c)Visual aspect produced by $A.1$ method (d)Visual aspect produced by B method.

4 Conclusion

In this work was evaluated two different inpainting approaches applied in the clouds removal field. The first approach is based in differential partial equations modeled by heat diffusion and by thin-plate spline. The second approach uses a multidimensional DCT-based smoothing method.

As showed in Table 1 as well in Table 2, the use of the thin-plate spline model did not achieved satisfactory results. Moreover, this method presented an unacceptable execution time. The $A.1$ method, based in heat diffusion, had a similar to the results achieved by the approach based in nearest neighbor interpolation. The visual aspect of these methods was also similar, where the B method was slight more efficient than $A.1$ method, generally.

These methods were applied to other images, that follows the same interpretation. In some instances, the $A.1$ method was superior than B method, but in most of the opportunities the B method presented better results in terms of PSNR and Kappa values, as well as more consistent visual appearance.

References

1. Bertalmio, M., Sapiro, G., Caselles, V., Ballester, C.: Image inpainting. In: Proceedings of the 27th annual conference on Computer graphics and interactive techniques. pp. 417–424 (2000)
2. Bookstein, F.: Principal warps: Thin-plate splines and the decomposition of deformations. IEEE Transactions on Pattern Analysis and Machine Intelligence 11, 567–585 (1989)
3. Buckley, M.: Fast computation of a discretized thin-plate smoothing spline for image data. Biometrika 81, 247–258 (1994)
4. Caselles, V., Haro, G., Sapiro, G., Verdera, J.: On geometric variational models for inpainting surface holes. Comput. Vis. Image Underst. 111, 351–373 (2008)

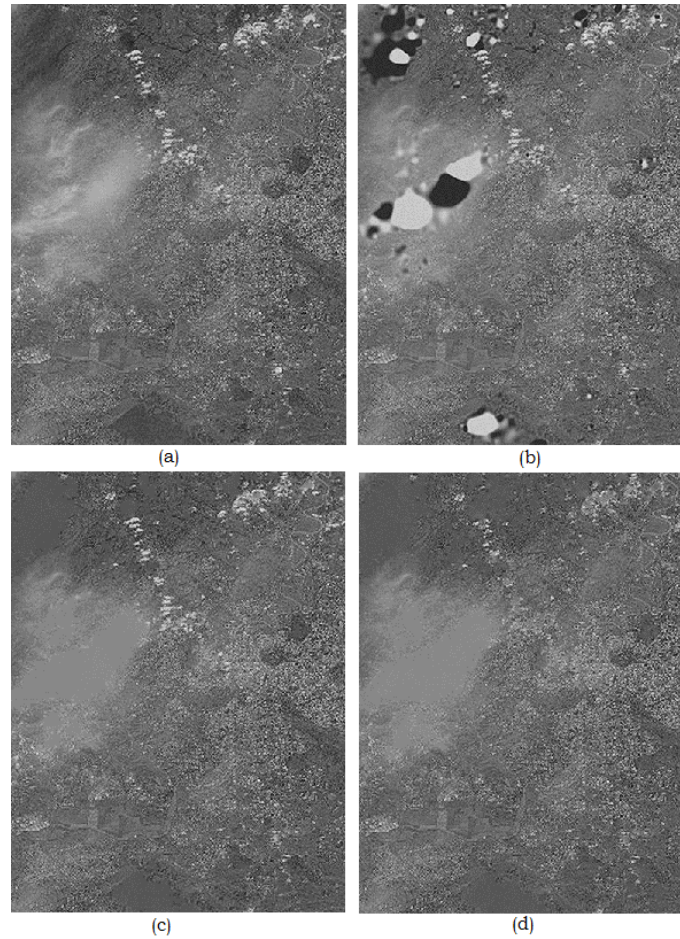


Fig. 13. (a)Image 9 of the Table 1 (b)Visual aspect produced by $A.2$ method (c)Visual aspect produced by $A.1$ method (d)Visual aspect produced by B method.

5. CASTANHO, J.E.C.: Registro de Imagens: uma solução para a modelagem de deformações e automação da correspondência. Ph.D. thesis, Universidade Estadual de Campinas (1997)
6. Chan, T.F., Shen, J.: Morphologically invariant PDE inpaintings. IEEE Transactions in Image Process (2001)
7. Chen, F., Suter, D.: Fast multipole method for accelerating the evaluation of splines. IEEE Comput. Sci. Eng 3, 24–31 (1998)
8. Criminisi, A., Pérez, P., Toyama, K.: Region filling and object removal by exemplar-based image Inpainting. In: IEEE Transactions on Image Processing. vol. 13, pp. 1200–1212 (2004)
9. DErrico, J.: Re interpolating over nans newsgroup comp soft-sys matlab (2003)
10. Garcia, D.: Robust smoothing of gridded data in one and higher dimensions with missing values. Computational Statistics & Data Analysis 54(4), 1167–1178 (2010)
11. Gonzalez, R.C., Woods, R.E.: Digital Image Processing. Addison-Wesley Publishing Company (2008)
12. Hale, D.: Image-guided blended neighbor interpolation of scattered data. 79th Annual International Meeting, Society of Exploration Geophysicists 28, 1127–1131 (2009)

13. Hau, C.Y., Liu, C.H., Chou, T.Y., Yang, L.S.: The efficacy of semi-automatic classification result by using different cloud detection and diminution method. *The International Archives of the Photogrammetry, Remote Sensing and Spatial Information Sciences* (2008)
14. Hoan, N.T., Tateishi, R.: Cloud removal of optical image using SAR data for ALOS applications. Experimenting on simulated ALOS data. *The International Archives of the Photogrammetry, Remote Sensing and Spatial Information Sciences* (2008)
15. Kresimir, M., G.M.G., D.: *Handbook Of Data Compression*. Springer (2009)
16. Kwok, T., Sheung, H., Wang, C.: Fast query for exemplar-based image completion. *IP* 19, 3106–3115 (2010)
17. Liu H., W.W., X., B.: Study of image inpainting based on learning. *Proceedings of The International MultiConference of Engineers and Computer Scientists* pp. 1442–1445 (2010)
18. Ma, J., Gu, X., Feng, C., Guo, J.: Study of thin cloud removal method for cbers-02 image. *Science in China Series E* 48 Issue: 2 (2005-03), 72–90 (2005)
19. Maalouf, A., Carre, P., Augereau, B., Fernandez Maloigne, C.: A bandelet-based Inpainting technique for clouds removal from remotely sensed images. *IEEE Transactions on Geoscience and Remote Sensing* 47(7), 2363–2371 (2009)
20. Magna Junior, J.P., Camargo, P.O., Galo, M.: O uso de thin-plate splines na modelagem de distorcoes entre sad69 e sirgas2000. *III Simposio Brasileiro de Ciencias Geodesicas e Tecnologia da Geoinformacao*. pp. 001–007 (2010)
21. Paragios, N., Chen, Y., Faugeras, O.: *Mathematical models in computer vision: the handbook*. Springer (2005)
22. Salomon, D., Motta, G.: *Handbook Of Data Compression*. Springer (2009)
23. Shen, H.F., Ai, T.H., Li, P.X.: Destriping and Inpainting of Remote Sensing Images Using Maximum A-Posteriori Method. In: *ISPRS 2008*. vol. XXXVII, pp. 63–70 (2008)
24. Shen, H., Liu, Y., Ai, T., Wang, Y., Wu, B.: Universal reconstruction method for radiometric quality improvement of remote sensing images. *International Journal of Applied Earth Observation and Geoinformation* 12(4), 278 – 286 (2010)
25. Siravenha, A.C., Sousa, D., Bispo, A., Pelaes, E.: The use of high-pass filters and the inpainting method to clouds removal and their impact on satellite images classification. In: *ICIAP (2)*. *Lecture Notes in Computer Science*, vol. 6979, pp. 333–342. Springer (2011)
26. Strang, G.: The discrete cosine transform. *SIAM Review* 41, 135–147 (1999)
27. Wang, Z., Zhou, F., Qi, F.: Inpainting thick image regions using isophote propagation. *Proceedings of International Conference on Image Processing - ICIP* pp. 689–692 (2006)
28. You, Y.L., Kaveh, M.: Fourth-order partial differential equations for noise removal. *Image Processing, IEEE Transactions on* 9(10), 1723 –1730 (2000)
29. Zhang, F., Xiao, Z., Ni, K., Xi, H.: Image restoration method based on the combination of heat conduction equation and anisotropic coupled diffusion equations. In: *Control, Automation and Systems Engineering (CASE)*, 2011 International Conference on. pp. 1–4 (july 2011)
30. Zhang, X., Qin, F., Qin, Y.: Study on the thick cloud removal method based on multi-temporal remote sensing images. In: *International Conference on Multimedia Technology (ICMT)*. pp. 1–3 (2010)



Ana Carolina Siravenha received her B.S. degree in Computer Engineering from Federal University of Para (2008) and the MSC. degree in Electrical Engineering from the Federal University of Para (2010). She is currently a Ph.D. student in Electrical Engineering at the Federal University of Para. Has experience in Electrical and Computer Engineering with emphasis in signal processing, mainly in the following areas: digital image processing, remote sensory images segmentation and classification, image restoration and Discrete Cosine Transform applied to classification.



Danilo Sousa received his B.S. degree in Computer Engineering from Federal University of Para, Belem, Brazil, in 2011. He is currently a MSC. student in the Post-Graduate Program in Electrical Engineering. His research interests are in digital image processing (image restoration, inpainting, segmentation and classification), remote sensing and Pattern Recognition.



Aline Bispo received her B.S. degree in Computer Engineering from Federal University of Para (2011). She is currently a MSC. student in Electrical Engineering working in image interpretation. She has experience in Electrical Engineering with emphasis in signal processing, mainly in the following areas: image restoration, pattern recognition strategies for image segmentation and classification of data.



Evaldo Pelaes received his B.S. degree in Electrical Engineering from Federal University of Para (1977), Full undergraduate degree in Physics from the Federal University of Para (1977), MSC. degree in Electrical Engineering from the Catholic University of Rio de Janeiro (1982) and Ph.D. in Electrical Engineering State University of Campinas (1998). He's currently an associate professor at the Federal University of Para and has experience in Electrical Engineering with emphasis in signal processing, mainly in the following areas: wavelet transform, image coding, propagation models, and mobile power quality.